AIAA JOURNAL
Vol. 35, No. 5, May 1997

# Numerical Simulation of Receptivity Phenomena in Transitional Boundary-Layer Flows

Scott H. Reitsma* and Vincent P. Manno†
*Tufts University, Medford, Massachusetts 02155*
and
Thomas F. Tureaud‡
*Charles Stark Draper Laboratory, Inc., Cambridge, Massachusetts 02139*

**A computational fluid-acoustic methodology is described and used to simulate induced and acoustic receptivity in unsteady boundary-layer flows. The methodology solves a finite compressibility form of the Navier–Stokes equations using a flux differenced, finite volume technique. Special attention is paid to nonreflective boundary conditions appropriate for unsteady, multidimensional problems including those involving viscous shear and propagating waves. The numerical experiments include the simulation of acoustic receptivity due to surface inhomogeneity in which the acoustic phenomena are modeled using physically appropriate wavelengths. Required steady solution accuracy, convergence acceleration techniques, boundary condition/flowfield interactions and the challenges of scale resolution vs computational cost are addressed in a series of simulations. The computed results are shown to be in agreement with linear stability theory and experimental measurements.**

## Nomenclature

$A$ = input disturbance amplitude
$\boldsymbol{A}_{x(y)}$ = Jacobian matrix of $x(y)$ flux vector
$a$ = $\frac{1}{2}$ extent of input disturbance
$a_{\mathrm{TS}}$ = average phase velocity of Tollmien–Schlichting wave
$\boldsymbol{C}$ = vector of pseudosource terms
$c$ = pseudospeed of sound, $\sqrt{(u^2+\beta)}$
$d$ = input disturbance center coordinate
$e$ = constant used in numerical bump prescription
$\boldsymbol{f}$ = $x$-direction flux vector
$\boldsymbol{f}_{+(-)}$ = $x$-direction cell face fluxes between cells $j$ and $j+1$ ($j-1$ and $j$)
$\boldsymbol{g}$ = $y$-direction flux vector
$\boldsymbol{g}_{+(-)}$ = $y$-direction cell face fluxes between adjacent cells
$k$ = acoustic wave number
$\boldsymbol{L}$ = left eigenvector matrix of $\boldsymbol{A}$
$\boldsymbol{L}_i$ = $i$th row (eigenvector) of $\boldsymbol{L}$
$L_{\mathrm{ref}}$ = reference length
$M$ = Mach number
$p$ = pressure
$p_s$ = acoustic source strength
$p_\rho$ = pressure parameter; see Eq. (1b)
$p_0$ = reference pressure
$\boldsymbol{q}$ = primitive variable vector
$\boldsymbol{R}$ = right eigenvector matrix of $\boldsymbol{A}$
$Re$ = Reynolds number
$t$ = time
$\boldsymbol{U}$ = velocity vector
$u$ = $x$-direction velocity component
$v$ = $y$-direction velocity component
$\boldsymbol{w}$ = characteristic variable vector, where $\delta\boldsymbol{w}$ is $\boldsymbol{L}\delta\boldsymbol{q}$
$w_i$ = $i$th element of $\boldsymbol{w}$
$x, y$ = coordinate directions
$x_c$ = centroid $x$ coordinate
$x_{\mathrm{cr}}$ = $x$ coordinate of critical $Re$
$y_1$ = grid stretching parameter
$\alpha_{\mathrm{TS}}$ = average spatial amplification rate of Tollmien–Schlichting wave
$\beta$ = finite compressibility factor
$\Delta x$ = cell size in $x$ direction
$\Delta y$ = cell size in $y$ direction
$\delta$ = boundary-layer thickness
$\delta\boldsymbol{q}$ = perturbation of $\boldsymbol{q}$ around linearized state
$\delta^*$ = displacement thickness
$\Lambda$ = diagonal matrix of eigenvalues of $\boldsymbol{A}$
$\lambda_i$ = $i$th eigenvalue of $\boldsymbol{A}$
$\lambda_{\mathrm{TS}}$ = Tollmien–Schlichting wavelength
$\rho_0$ = reference density
$\phi$ = idealized two-dimensional characteristic variable vector
$\phi_i$ = $i$th element of $\phi$
$\omega$ = frequency

*Subscripts*

$v$ = viscous fluxes
wall = input disturbance

Received Aug. 17, 1995; revision received Dec. 9, 1996; accepted for publication Jan. 22, 1997. 

*Research Assistant, Department of Mechanical Engineering; currently Engineer, Polaroid Corporation, Waltham, MA 02154.
†Associate Professor, Department of Mechanical Engineering.
‡Technical Staff Member, Department of Mechanical Engineering; currently Engineer, VCT, Inc., Fairfax, VA 22030. Member AIAA.

## I. Introduction

THE ability to simulate low Mach number, fluid-acoustic phenomena has both theoretical and practical importance. Fundamental topics include flow transition and stability theory, solution methodologies for pseudohyperbolic mathematical systems, and advancement of computational fluid dynamics (CFD) techniques. Practical applications include boundary-layer control for lift and drag manipulation, as well as sensor self-noise, edgetone, and cavity signatures and radiated noise patterns. The most vexing problems involve turbulent flow such as characterizing a priori the frequency and wave number spectra of noise generated by turbulent flow over flat and curved surfaces.[1]

In a compilation of outstanding questions in fluid mechanics, Morris and McLaughlin[2] summarize fundamental questions about the physical mechanisms of sound generation in low Mach number turbulent flows. Understanding these physical connections at low Mach numbers is difficult due to the range of relevant time and length scales (vortical structures, instabilities, and pressure waves). The connection between the organized structures of unsteady flow and sound generation are poorly understood even though Lighthill's[3] analogy has allowed the solution of many practical fluid-acoustic problems. Morris and McLaughlin[2] and others[4,5] argue that

numerical simulation, computational fluid acoustics (CFA), may offer a fruitful path to uncovering these connections.

A prerequisite to simulating turbulent fluid-acoustic problems is accurate prediction in the transitional flow regime. This paper utilizes a first principles approach to model boundary-layer receptivity. Receptivity is an appropriate problem for CFA benchmarking due to its physical complexity.[6–10] Performing CFA numerical experiments shares many of the difficulties, which Nishioka and Morkovin[10] note in the design and performance of repeatable and credible physical experiments. Length and time scales differ by orders of magnitude and successful experiments require the resolution of low-amplitude perturbation parameters to track the observed phenomena. The simulation work of Fasel[11,12] and the experimental work of Saric et al.[13] are particularly relevant to this work.

## II. Methodology

### A. Conservation Equations

The conservation equations used are similar to the pseudocompressible form of the Navier–Stokes equations.[14] A detailed discussion of the utility of this formulation in regimes of interest is given by Manno et al.[15] The dimensionless conservation equations have the following form for a two-dimensional, Cartesian coordinate system:

$$\frac{\partial \boldsymbol{q}}{\partial t}+\frac{\partial \boldsymbol{f}}{\partial x}+\frac{\partial \boldsymbol{g}}{\partial y}=\frac{1}{Re}\left[\frac{\partial \boldsymbol{f}_v}{\partial x}+\frac{\partial \boldsymbol{g}_v}{\partial y}\right] \tag{1a}$$

where

$$\boldsymbol{q}=\begin{vmatrix} p_\rho \\ u \\ v \end{vmatrix}, \qquad \boldsymbol{f}=\begin{vmatrix} \beta u \\ p+u^2 \\ uv \end{vmatrix}, \qquad \boldsymbol{g}=\begin{vmatrix} \beta v \\ uv \\ p+v^2 \end{vmatrix}$$

$$\boldsymbol{f}_v=\begin{vmatrix} 0 \\ \dfrac{\partial u}{\partial x} \\ \dfrac{\partial v}{\partial x} \end{vmatrix}, \qquad \boldsymbol{g}_v=\begin{vmatrix} 0 \\ \dfrac{\partial u}{\partial y} \\ \dfrac{\partial v}{\partial y} \end{vmatrix}, \qquad \text{and} \qquad p_\rho=\frac{p-p_0}{\rho_0} \tag{1b}$$

The 0 subscript indicates reference states, and $\beta$ is the finite compressibility factor. The correct physical value of $\beta$ is $1/M$ as opposed to lower, computationally convenient values typical of pseudocompressibility solutions. This equation set will resolve unsteadiness due to compressibility effects to an accuracy of $\mathcal{O}(M)$ (Ref. 16).

### B. Numerical Solution

These conservation equations are solved using the time accurate Navier–Stokes (TANS) code.[16] TANS was developed using the David Taylor Navier–Stokes code[17] as a foundation in terms of data structure, numerical approximation, and solution control. However, the modifications and additions are substantive, and TANS should be considered as a distinct software package. TANS employs a finite volume discretization. Viscous terms are approximated using central differencing. The convective terms are discretized using a third-order, upwind biased, flux differenced splitting algorithm. The discretized form of the conservation equations has the form

$$\Delta x \Delta y \frac{\partial \boldsymbol{q}}{\partial t}+\Delta y[\boldsymbol{f}_+ - \boldsymbol{f}_-]+\Delta x[\boldsymbol{g}_+ - \boldsymbol{g}_-]=\mathbf{RHS} \tag{2}$$

where RHS is the right-hand side. The cell face fluxes are estimated from the local Riemann solution in which the flux transition parameters are calculated using Roe averaging.[18]

There are two time advancement options. An explicit, three-step, second-order Runge–Kutta algorithm is used for transiently accurate computations. Second-order time accuracy is sufficient because of the small time steps imposed to resolve acoustic time scales. The three-step procedure is used because of its improved stability range. An implicit, approximate factorization, time advancement is used only to accelerate convergence to pretransient steady-state conditions.

### C. Boundary Condition Specification

In CFA analysis, near-field computational boundaries are necessary in order to reduce the computational domain to a manageable size. These boundaries must maintain physically reasonable unsteady bulk flow motion and ensure that outgoing acoustic waves and other disturbances (e.g., vortical) are not reflected. It is particularly important to avoid nonphysical reflections in transitional flow simulations, as these reflections could influence the evolution of physical instabilities in the computational domain.[10] Conversely, CFA boundary conditions must admit imposed disturbances without wave distortion due to impedance mismatches.

Equation (1) defines a partial differential equation system, which is parabolic–hyperbolic in nature, and hence the system is characterized by a complex eigensystem. When expressed in quasilinear form and neglecting (for the moment) viscous contributions, Eq. (1) can be written as

$$\frac{\partial \boldsymbol{q}}{\partial t}+\boldsymbol{A}_x\frac{\partial \boldsymbol{q}}{\partial x}+\boldsymbol{A}_y\frac{\partial \boldsymbol{q}}{\partial y}=0 \tag{3}$$

where $\boldsymbol{A}_x$ and $\boldsymbol{A}_y$ are the flux Jacobians in the $x$ and $y$ directions, respectively. The specific forms of $\boldsymbol{A}_x$ and $\boldsymbol{A}_y$ are

$$\boldsymbol{A}_x=\frac{\partial \boldsymbol{f}}{\partial \boldsymbol{q}}=\begin{vmatrix} 0 & \beta & 0 \\ 1 & 2u & 0 \\ 0 & v & u \end{vmatrix} \quad \text{and} \quad \boldsymbol{A}_y=\frac{\partial \boldsymbol{g}}{\partial \boldsymbol{q}}=\begin{vmatrix} 0 & 0 & \beta \\ 0 & v & u \\ 1 & 0 & 2v \end{vmatrix} \tag{4}$$

For example, the $x$-direction, inviscid Jacobian matrix $\boldsymbol{A}_x$ can be decomposed as

$$\boldsymbol{A}_x=\boldsymbol{R}_x\boldsymbol{\Lambda}_x\boldsymbol{L}_x \tag{5}$$

where

$$\boldsymbol{R}_x=\begin{vmatrix} 0 & [(c-u)/2c] & [(c+u)/2c] \\ 0 & 1/2c & -1/2c \\ -1/c^2 & v/c^2 & -v/c^2 \end{vmatrix} \tag{6}$$

$$\boldsymbol{\Lambda}_x=\begin{vmatrix} u & 0 & 0 \\ 0 & (u+c) & 0 \\ 0 & 0 & (u-c) \end{vmatrix}, \quad \text{and} \quad \boldsymbol{L}_x=\begin{vmatrix} v & uv & -c^2 \\ 1 & (u+c) & 0 \\ 1 & (u-c) & 0 \end{vmatrix}$$

where $c=\sqrt{(u^2+\beta)}$. An analogous eigensystem can be defined for the $y$ direction.

The pseudohyperbolic nature of the conservation equations suggests that characteristic-based boundary conditions are appropriate.[19–21] Along any given direction, the conservation equations can be transformed from physical variables ($\boldsymbol{q}$) to characteristic variables ($\boldsymbol{w}$). This latter form makes clear in which direction waves are propagating. Outward propagating waves are defined entirely by the variable state within the computational domain and, hence, should not be used to provide boundary condition information. Conversely, waves propagating into the computational domain carry all boundary condition information.

Boundary conditions based on characteristic theory are strictly applicable to purely hyperbolic conservation equation sets in which directional characteristics can be decoupled. The finite compressibility conservation equations, even in the inviscid limit, remain coupled with respect to directional flux transport. With viscosity included, the equations yield a complex rather than a real eigensystem. Thus, the simple wavelike solutions of hyperbolic equations must be replaced by damped wave solutions, which are not accommodated by characteristic theory.

Reitsma et al.[22] describe a novel approach for dealing with this problem, which incorporates transverse gradients and viscous effects into nonreflective characteristic-based boundary conditions. Transverse gradients in a linearized reference state are maintained by prescribing the appropriate variation of the normal characteristic. Viscous momentum transport corrections are applied because this additional parabolic transport mechanism affects the data variation along characteristic line transport.

The approach of Reitsma et al.[22] is a generalization of the ideas advanced by Thompson[23] in which direction-specific Riemann variants of the form ($x$ direction shown)

$$d\phi = \boldsymbol{L}\, d\boldsymbol{q} + \boldsymbol{LC}\, dt \tag{7}$$

where $\boldsymbol{C}$ includes the transverse gradient effects ($\partial/\partial y$ in $x$-direction transport),

$$\boldsymbol{C} = \boldsymbol{A}_y \frac{\partial \boldsymbol{q}}{\partial y} = \begin{vmatrix} \beta \dfrac{\partial v}{\partial y} \\ v\dfrac{\partial u}{\partial y} + u\dfrac{\partial v}{\partial y} \\ \dfrac{\partial p}{\partial y} + 2v\dfrac{\partial v}{\partial y} \end{vmatrix} \tag{8}$$

are employed. A nonreflective condition, based on a locally linear solution, can be achieved if the incoming characteristic information is imposed as

$$\frac{\partial \phi_i}{\partial t} + \lambda_i \frac{\partial \phi_i}{\partial x} = \boldsymbol{L}_i \frac{\partial \boldsymbol{q}}{\partial t} + \lambda_i \boldsymbol{L}_i \frac{\partial \boldsymbol{q}}{\partial x} + \boldsymbol{L}_i \boldsymbol{C} = 0 \tag{9}$$

at the boundaries. In Thompson's formulation, the transverse gradient effects are associated with the other spatial gradients. Inasmuch as there is no physical basis to favor this association, the approach used in this work is to split this influence evenly between the spatial and temporal domains. Previously reported results using this approach have been shown to be superior in terms of accuracy and solution stability and more useful in finite volume formulations.[16,22] This approach is computationally efficient, admits properly the incoming characteristics associated with the steady reference solution, and achieves second-order nonreflection of outgoing disturbances.

In practice, this characteristic-based approach, although achieving very good nonreflection in the case of acoustical disturbances, does not adequately damp boundary reflections due to the transport of vortical disturbances through the computational boundaries. Therefore, an exit zone approach is also employed at certain boundaries to damp the outgoing vortical disturbances through grid-dependent numerical dissipation.[24]

## III. Simulations

This CFA methodology has been applied to a series of numerical experiments of increasing complexity.[16,22,25] The computations reported herein involve small-amplitude (i.e., linear regime) boundary-layer instability and receptivity phenomena. These phenomena are associated with the transition process by which a laminar flow becomes turbulent. Transition in boundary-layer flows requires two elements, a source of instability and a receptivity site in the flow to that instability.[8] Positive spatial amplification requires that the instigating disturbance be within unstable length scales and frequencies. The unstable ranges are strong functions of Reynolds number, surface geometry, and bulk flow pressure gradients. In flat plate geometries there are two regions that are characterized by positive instability amplification: near the leading edge and downstream of the location of neutral stability ($Re_{\delta^*} \approx 1000$).

In the first transition stage, called receptivity, external disturbances generate instability waves within the boundary layer. Acoustic receptivity involves the conversion of a long wavelength acoustic disturbance to a short wavelength convective disturbance. If these convected disturbances occur at particular wavelength and frequency combinations, they will amplify linearly to become the second stage of transition modeled accurately using the Orr–Sommerfeld equation. When the disturbances have been amplified sufficiently for nonlinear effects to become important, the final stage of transition causes the generation of nonintegral modes and the eventual breakdown into chaotic turbulent flow.

The present work focuses on the first two stages: receptivity and linear amplification. The results are divided into two subsections: amplification of disturbances introduced within the boundary layer, which will be termed induced receptivity, and acoustic receptivity. Acoustic receptivity implies the complete receptivity sequence of an external disturbance penetrating to the near-wall region and the subsequent local readjustment of disturbance wavelengths and amplification. This readjustment has been shown to occur if surface inhomogeneities are present.[7]

The calculations are compared to the experimental measurements of Saric et al.[13] The tests, which Saric et al.[13] describe as being similar to experiments performed in the former U.S.S.R. in the late 1970s, involved an airflow (freestream velocity $\approx$ 12.8 m/s or $M \approx 0.038$) over a flat plate 1.4 m wide, 0.0206 m thick, and 3.7 m long with an elliptical (67:1) leading-edge section. A speaker was mounted upstream of the plate to act as the external acoustic excitation source. The speaker produced a nearly planar wave with a sound level of 90–100 dB in the test section. Here, 90 dB corresponds to an acoustic $u'_{\text{rms}}$ level of approximately 0.016% of the freestream velocity. The sound frequency was 75.8 Hz, which translates to an acoustic wavelength of approximately 4.5 m. In contrast, the most unstable Tollmien–Schlichting (T–S) waves had wavelengths of roughly 0.05 m.

### A. Induced Receptivity

This subsection describes the computed amplification of nonacoustic input instabilities downstream of the neutral stability point. The disturbances are prescribed as boundary conditions that have a frequency and wavelength within the unstable range and a wavelength similar to the expected unstable T–S waves. The amplification of these instabilities is then compared to linear theory predictions. An additional validation step is to vary the length and time scales of the input disturbances to verify that stable disturbances are not amplified.

#### *1. T–S Waves*

The computational domain, shown in Fig. 1, is employed in this set of simulations. The computational domain spans the physical coordinates of $x = 0.307$–$0.970$ m, which is approximately 12 T–S wavelengths ($\lambda_{TS} = 0.054$ m). The neutral stability location $x_{cr}$ is at $x = 0.46$ m, which is 0.153 m downstream of the upstream boundary of this truncated domain. The upper boundary is at $y/L_{\text{ref}} = 0.03187$, which corresponds to approximately eight boundary-layer thicknesses at $x_{cr}$. $L_{\text{ref}}$ is set to 1.0 m. The minimum grid spacing in the $y$ direction is $\Delta y/L_{\text{ref}} = 0.000144$ or about $1/27\delta$ at the $x_{cr}$. A hyperbolic tangent stretching function is used to expand the grid spacing in the vertical direction. The stretching function maintains a nearly constant grid spacing through the boundary layer and rapidly expanding grid spacing above the boundary layer. The grid spacing $(\Delta x/L_{\text{ref}})_{\min}$ in the $x$ direction for all but the exit zone region is set to 0.001275 or $\frac{1}{42}$ of $\lambda_{TS}$. The exit zone uses a hyperbolic tangent stretching function to increase the cell size in the $x$ direction. The grid, including exit zone, contains a total of 30,345 (595 × 51) cells.

The Blasius solution is used as the reference state in the characteristic-based boundary conditions. The unperturbed upstream (left-hand side) boundary condition corresponds to the Blasius profile with $Re_{\delta^*} = 829$. A nonreflective outflow boundary condition was imposed downstream of the exit zone (right-hand side). The boundary condition on the top sets the $u$ and $v$ velocity gradients to zero with the pressure calculated from the appropriate characteristic compatibility relations.

Similar to Asai et al.,[26] the disturbance was introduced as an oscillating slip horizontal velocity at the wall given by

$$\begin{aligned} x < d - a \qquad & u_{\text{wall}} = 0 \\ d - a < x < d + a \qquad & u_{\text{wall}} = A\cos^2[(\pi/2)(x-d)/a]\sin\omega t \\ d + a < x \qquad & u_{\text{wall}} = 0 \end{aligned} \tag{10}$$

where disturbance amplitude $A = 0.01$, $d = 0.46$ m, and $\omega$ is the nondimensional disturbance frequency.

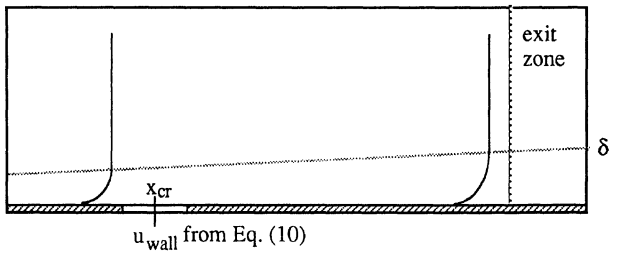


**Fig. 1 Computational domain for induced receptivity simulations.**

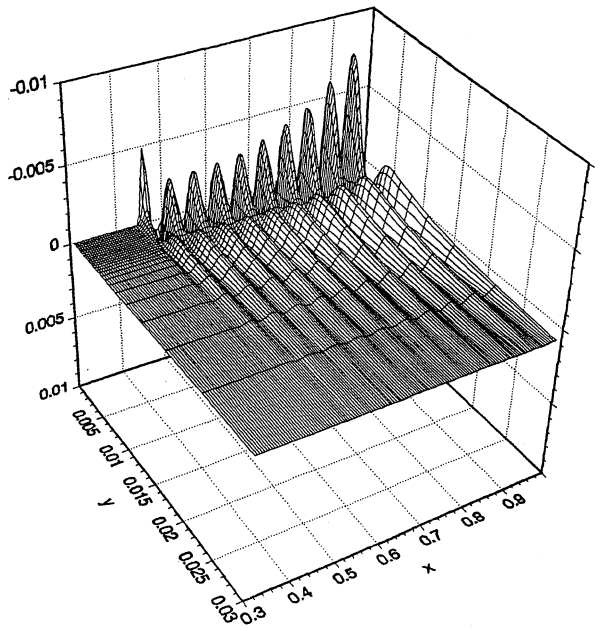


**Fig. 2 Unsteady portion of $u$ velocity ($u'$) at dimensionless time $t = 1.67$.**

The solution is computed in two parts. First, a converged steady solution is achieved by setting the amplitude of the disturbance $A$ to zero. Once an acceptable steady solution is calculated, this resultant flowfield is used as the initial conditions for the induced T–S wave simulation. The explicit time advancement with Courant–Friedrichs–Lewy number (CFL) equal to 1.8 (using $c$ as velocity) is used. The finite compressibility parameter $\beta$ is set to 100, which corresponds to $M = 0.1$. This is somewhat higher than the experimental value of the Mach number, but this does not affect this set of computations (see next subsection).

Figure 2 shows the computed unsteady portion of the $u$-velocity component ($u - u_{\text{steady}}$), a nondimensional time of 1.67 using a disturbance extent of $1/2\lambda_{TS}$ (0.0255 m), and a frequency $\omega$ of 37.354. These values correspond to a disturbance that has a branch I neutral stability point at $x = 0.46$. The amplification is evident just downstream of the input disturbance position. Note that, consistent with T–S wave theory, the velocity perturbation spatial distribution undergoes a phase shift at the outer edge of the boundary layer. During the computation, the T–S waves pass through the downstream boundary for several periods without reflection. This was expected because the T–S waves are disturbances oriented normal to the computational boundary. As noted earlier, the nonreflective boundary condition treatment derived as part of this work is well suited for such situations. Reitsma[16] reports reflections of less than 0.01% (based on amplitude) for such situations.

A quantitative comparison with linear theory is presented based on Orr–Sommerfeld equation solutions given by Obremski et al.[27] The comparisons shown in Table 1 were made by computing average values between $x = 0.6$ ($Re_\delta = 1160$) and $x = 0.9$ ($Re_\delta = 1420$). Obremski et al.[27] used a series solution approach to solving the instability equations for various favorable and adverse pressure gradients in flat plate geometries. The reported uncertainties in the linear theory entries in Table 1 are due to resolution of the graphical reports of the solutions.[27] Given that these solutions are used as benchmarks for more recent numerical solutions to the Orr–Sommerfeld equations and also noting the agreement achieved, independent numerical solution of the Orr–Sommerfeld equations were not performed.

In Table 1, $a_{TS}$ is the average phase velocity of the T–S wave, $\alpha_{TS}$ is the average spatial amplification rate of the T–S, $y_{max}$ is the location of maximum amplitude, and $y_{min}$ is the location of the velocity profile phase shift.

*2. Disturbance Length and Time Scale Effects*

To complete the induced receptivity validation, the code was run to confirm that the model does not amplify stable disturbances. In one case, the wavelength of the input disturbance was increased 10 times ($2a = 5\lambda_{TS}$). Such a disturbance falls far outside of the thumb curve and was quickly damped in the simulation. In another case, the frequency of the disturbance was increased 10 times. Again, this disturbance should be quickly damped, and the numerical results correctly showed this behavior.

**Table 1 Comparison of simulated T–S wave characteristics with linear theory**

| | Linear theory | TANS code |
|---|---|---|
| $\lambda_{TS}$ | 0.054 | 0.0545 |
| $\omega_{TS} L/U_0$ | 37.354 | 37.3 |
| $a_{TS}/U_0$ | $32 \pm 0.5$ | 32.3 |
| $\alpha_{TS}$ | $3.0 \pm 0.75$ | 2.53 |
| $y_{max}/\delta$ | $0.2 \pm 0.05$ | 0.18 |
| $y_{min}/\delta$ | $0.8 \pm 0.05$ | 0.73 |

### B. Acoustic Receptivity

In acoustic receptivity problems, sound energy external to the boundary layer is the instability source. In low Mach number problems, the acoustic waves have wavelengths approximately two orders of magnitude greater than those associated with the T–S waves. From a process perspective, acoustically induced boundary-layer transition requires an external acoustic disturbance, a receptivity site providing a short streamwise scale readjustment region such as an adverse pressure gradient or surface inhomogeneity, and the proper boundary-layer characteristics, which amplify the local disturbance. Just as the freestream flow undergoes a transition in the boundary layer to match the no-slip condition, the freestream acoustic disturbance undergoes a transition similar to an inverse Stokes layer. The thickness of this Stokes layer is about $1/3\delta$ at $x_{cr}$. The local readjustment of the Stokes layer near surface inhomogeneities is believed to be the mechanism that produce unstable disturbances within the boundary layer.[7]

The flow is receptive if surface inhomogeneities of the proper length scale are present. Acoustic waves moving parallel to a flat surface represent the least efficient orientation for acoustic receptivity. As such, a length scale readjustment must be introduced. In the physical experiment, this was accomplished by placing very thin Mylar® tape (0.0001 m thick, 0.025 m long) at the expected neutral stability location. This location is well past the region of leading-edge instability phenomena. Saric et al.[13] found that the upstream acoustic source did not induce measurable T–S waves if the Mylar strip was not present. The imposition of the thin strip instigated T–S waves with amplitude and phase behavior in close agreement with linear theory. Induced instability wave amplitude also increased with strip height. This increase was linear at lower energy forced disturbances (<100 dB) but showed a nonlinear response at higher levels (>100 dB).

*1. Computational Problem Definition*

CFA calculations challenge standard CFD procedures. The relevant physical phenomena are small perturbations, and hence, the numerical solution must be very clean to resolve these perturbations. This is further exacerbated by the fact that the problem is physically unstable, and small numerical glitches can be amplified by the physical instability mechanisms. Special care must be taken in the description of geometries and the imposition of boundary conditions.

A computational domain schematic for the acoustic receptivity simulation includes the leading edge, as is shown in Fig. 3. The physical leading edge was a 67:1 ellipse, which joined smoothly to the flat plate at $x = 0.34$ m. For the numerical simulation, a 6700:1 ellipse was chosen to facilitate gridding within a single zone. This change is acceptable because leading-edge effects are negligible whenever the elliptical ratio is 24:1 or greater.[28]

Certain compromises were made to keep the problem within the limitations of available computer resources (limited Cray C90 CPU time). The first involved the shape of the Mylar tape bump. An accurate representation of the discontinuous nature of the height change would require an excessively fine grid. Because increased grid resolution was not computationally affordable, it was necessary

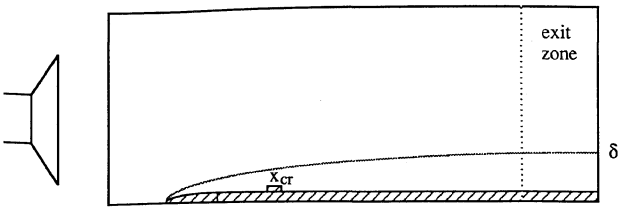


**Fig. 3 Computational domain for acoustic receptivity problem.**

) approximate this strip or bump with the smoother geometry described by

$$\frac{y_{\text{bump}}}{L_{\text{ref}}} = \frac{0.0001 y_1}{y_1 + (x - 0.46)^6} \tag{11}$$

/here $y_1 = 7.164369 \times 10^{-12}$. $L_{\text{ref}}$ is 1.0 m. The numerical bump preads the transition from $y/L_{\text{ref}} = 0.0000$ to 0.0001 over a horiontal distance of more than 10 bump heights. It was realized a priori ıat the smoothness of the numerical bump would reduce the magniıde of the simulated receptivity. The second compromise involved ıe vertical discretization. Whereas the grid adequately resolved the iscous boundary layer and developing T–S waves, it did not resolve ıe inverse Stokes layer with great precision. This further decreased ıe magnitude of receptivity in the numerical simulation.

The final compromise concerned the value of $\beta$. The freestream Aach number in the physical experiment was 0.0375 or $\beta = 711$. Because $\Delta t$ is inversely proportional to $\sqrt{\beta}$, this would produce a ery restrictive time step limitation. Instead, the simulations were erformed using $\beta = 100$ ($M = 0.1$). In effect, the computaional fluid had the viscosity and density of air but a speed of sound qual to roughly 38% of the physical value. Hence, the acoustic vavelengths were decreased somewhat from their physical values ut remained approximately 30 times longer than $\lambda_{TS}$. Also, seting $\beta = 100$ causes the pressure variation associated with a given coustic velocity variation to be 2.7 times smaller than its physical alue, which further decreases receptivity.[8,29] Note that these comromises were due to resource limitations and are not indicative of nethodological weaknesses.

The computational domain spans $x/L_{\text{ref}} = -0.846$ to 1.444. Reynolds number based on $L_{\text{ref}}$ was 757,125. The upper boundary t $y/L_{\text{ref}} = 0.03187$ corresponds to approximately $8\delta$ at $x_{cr}$. The ninimum grid spacing in the $y$ direction $(\Delta y/L_{\text{ref}})_{\min}$ is 0.000144 r about $1/27\delta$ at $x_{cr}$. A hyperbolic tangent stretching function is sed in the vertical direction. The grid stretching function maintains nearly constant cell size through the boundary layer and expands airly rapidly above the boundary layer. The grid spacing in the $x$ irection reduces smoothly from 0.04 (normalized to $L_{\text{ref}}$) at the nflow boundary to 0.004 at the leading edge and 0.000567 at the ump. After the bump, the spacing expands to 0.001275 or roughly $\frac{1}{2}$ of $\lambda_{TS}$ and remains at that value until the exit zone. The grid pacing upstream of the bump is larger because the smallest relevant ength scale in that region is the acoustic wavelength. No attempt was nade to resolve the leading-edge instabilities. The leading edge flow vas resolved adequately to yield accurate bulk flow results farther lownstream. The exit zone uses a hyperbolic tangent stretching unction in the $x$ direction. The grid, including exit zone, contains total of 65,025 (1275 × 51) cells.

The outflow (right) and top horizontal boundary conditions are dentical to those used in the previous calculations. The lower horzontal boundary is a no-slip condition on the plate and a symnetry condition upstream of the plate. The inflow (left) boundary ondition is a nonreflective condition, which includes the acoustic ource:

$$u = 1 + A\cos(kx - \omega t)$$
$$p_\rho = 1 + (A\omega/k)\cos(kx - \omega t) \qquad \text{and} \qquad v = 0 \tag{12}$$

where $\omega$ is the acoustic frequency (i.e., speaker frequency).

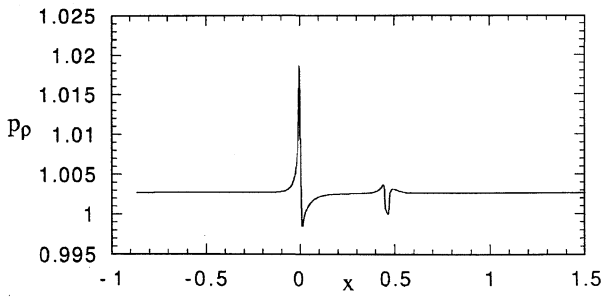


**Fig. 4 Steady pressure profile $p_\rho$ at $y/L_{\text{ref}} = 0.00078$.**

*2. Achieving an Acceptable Steady State*

A converged, instability free, steady state must first be established. This is accomplished by setting $A$ in Eq. (12) to 0. This steady state provides a baseline against which to compare the unsteady solutions. The first few thousand time steps were performed using the implicit algorithm with CFL = 60. The residuals decreased as expected over the first 4000 steps but then began to rise. An examination of the solution showed that an unsteadiness quite similar in behavior to a T–S wave was being generated upstream of the surface inhomogeneity. Additional implicit calculations at lower CFL numbers (down to CFL = 1.8) showed that this same phenomenon, though with lower amplitudes, persisted in all implicit calculations. It is postulated that the implicit field solution creates a global instability from what should be a convective instability. When the calculation was restarted using the explicit Runge–Kutta method and a CFL = 1.8, the nonphysical instability waves generated during the implicit stage convected out of the solution domain leaving a converged, instability free, steady state. This two-stage convergence strategy of using implicit time advancement to converge quickly to an approximate solution and then using explicit time advancement to eliminate low amplitude but no insignificant unsteadiness is computationally expensive. Unfortunately, no practical alternative to it was found.

The steady pressure profile at $y/L_{\text{ref}} = 0.00078$ is shown in Fig. 4. Upstream and downstream of the bump this corresponds to a nondimensional elevation of $y/L_{\text{ref}} = 0.00078$ above the surface of the plate while it corresponds to the seventh finite volume cell above ($y$ direction) the bump.

*3. Unsteady Calculations*

The acoustic source strength at the inflow boundary was set to the same $u'$ rms measured in the physical experiment (0.016% of $U_0$). The simulation was restarted using the steady results as the initial conditions. To avoid a sudden disturbance to the solution, the acoustic source amplitude was ramped linearly to its final value over the initial 1000 time steps.

The pressure profile after 131,000 time steps (3.364 nondimensional time units) is shown in Fig. 5. This profile is similar the steady solution (Fig. 4) with a superimposed, long wavelength acoustic wave. Figures 6 and 7 show the pressure and $u$-velocity perturbation values (steady solution subtracted from the $t = 3.36$ solution). The developing T–S wave is easily visible. The steady pressure disturbances at the leading edge and at the bump are unchanged by the acoustic wave and cancel when calculating the perturbation. In agreement with theory, the acoustic wave produces a local readjustment of the velocity field at the leading edge and at the bump (see Fig. 8). The local readjustment has the proper frequency and wavelength characteristics to trigger an unstable response. In agreement with linear theory, the local disturbance at the leading edge is quickly damped, but the disturbance at the bump (neutral stability location) is amplified.

Subtracting the superimposed inverse Stokes wave from the solution makes the analysis of the T–S waves more straightforward. This was accomplished by recording the state of the computational domain at an earlier time but at the same phase of the acoustic cycle. After 13,121 steps (dimensionless $t = 0.336$), the acoustic wave has traveled the length of the computational domain but the slower moving T–S wave has barley begun to develop. Subtracting the $t = 0.336$ solution from the $t = 3.364$ solution effectively

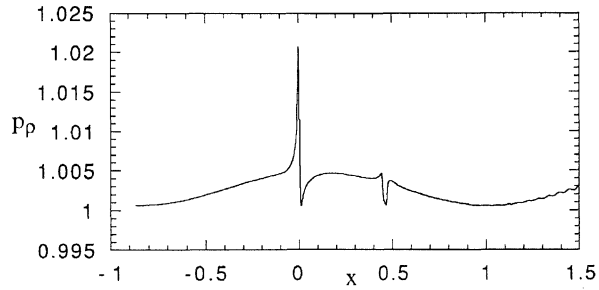


**Fig. 5 Pressure profile $p_\rho$ at $y/L_{\text{ref}} = 0.00078$, $t = 3.364$.**

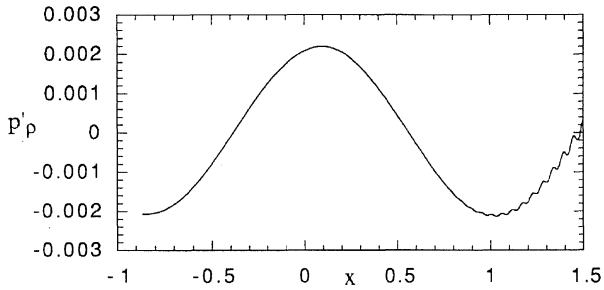


**Fig. 6 Pressure perturbation profile $p_\rho$ at $y/L_{\text{ref}} = 0.00078$, $t = 3.364$.**

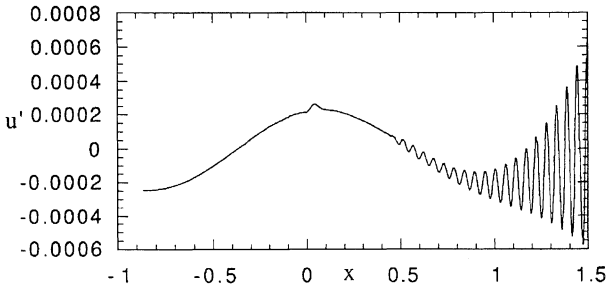


**Fig. 7 Perturbation profile of $u$ velocity ($u'$) at $y/L_{\text{ref}} = 0.00078$, $t = 3.364$.**

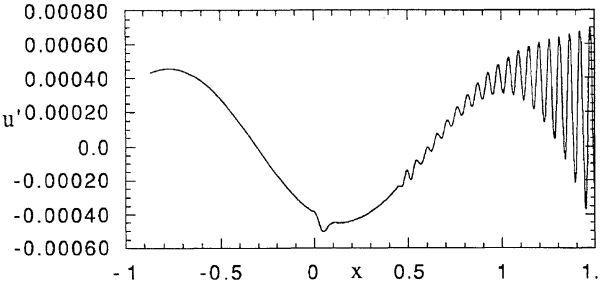


**Fig. 8 Perturbation profile of $u$ velocity ($u'$) at $y/L_{\text{ref}} = 0.00078$, $t = 3.461$.**

eliminates the steady and acoustic components and leaves only perturbations due to the T–S wave.

Figure 9 shows the $u$-velocity perturbation associated with the T–S wave. The exponential growth of the T–S wave is evident. The $u'$ profile of the T–S wave in the vertical plane at $(x/L_{\text{ref}}) = 1.445$ and $t = 3.364$ is shown in Fig. 10. Figure 11 shows the $u$-velocity T–S perturbation over a large section of the computational domain. The characteristic phase shift toward the outer edge of the boundary layer can be seen. These results show that the qualitative aspects of boundary-layer receptivity have been simulated. Table 2 presents a quantitative comparison to the experimental values and the predictions of linear theory. The simulation compares quite well in most respects. The largest discrepancy is the amplitude of the combined disturbance (T–S waves and Stokes wave) given by $u'_{\text{rms}}$. As already discussed, this reduced level of receptivity was anticipated.

**Table 2 Comparison of simulated T–S waves with linear theory and experiment**

| | Experiment | Linear theory | TANS code |
|---|---|---|---|
| $\lambda_{\text{TS}}$ | 0.054 | 0.054 | 0.054 |
| $\alpha_{\text{TS}}/U_0$ | — | $32 \pm 0.5$ | 33 |
| $\alpha_{\text{TS}}$ at $x = 1.32$ | — | $3.7 \pm 0.75$ | 3.2 |
| $\max u'_{\text{rms}}/U_0$ | 0.11 | — | 0.042 |
| $y_{\max}/\delta$ | $0.14 \pm 0.02$ | $0.12 \pm 0.01$ | 0.11 |
| $y_{\min}/\delta$ | $0.57 \pm 0.05$ | $0.68 \pm 0.01$ | 0.67 |

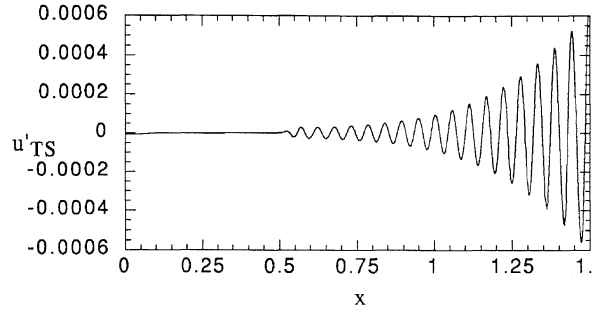


**Fig. 9 T–S perturbation profile of $u$ velocity ($u'_{\text{TS}}$) at $y/L_{\text{ref}}$ 0.00078, $t = 3.364$.**

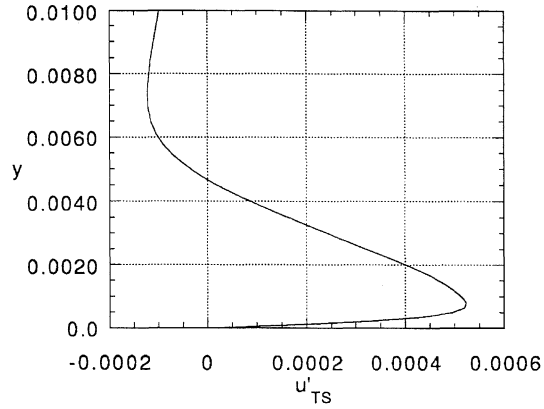


**Fig. 10 T–S vertical ($y$) perturbation profile of $u$ velocity ($u'_{\text{TS}}$) $x/L_{\text{ref}} = 1.4444$, $t = 3.364$.**

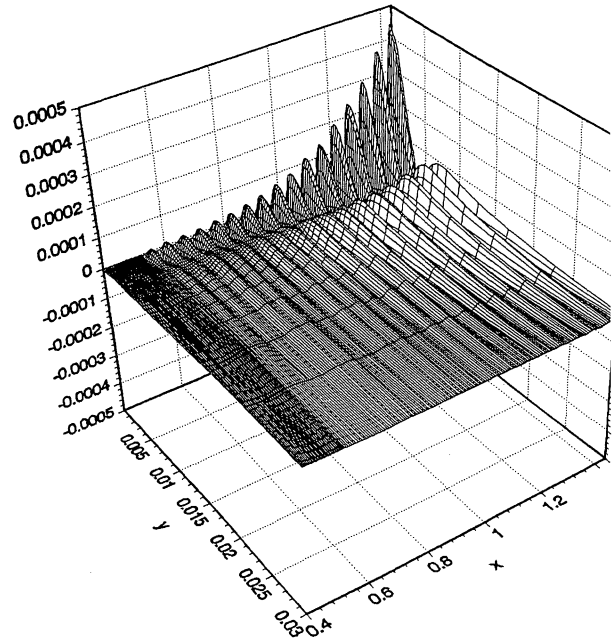


**Fig. 11 T–S wave perturbation profile of $u$ velocity ($u'_{\text{TS}}$) at $t = 3.3$**

The numerical simulation was repeated using a stronger acoustic disturbance (100 dB). The $u'_{rms}$ associated with this acoustic wave is 0.0384% $U_0$, 2.40 times larger than the previous simulation. The experiments and triple deck theory[7] predict that the receptivity magnitude should increase linearly with the acoustic disturbance. The increase in the simulated T–S wave amplitude was a factor of 2.40, as predicted.

Another case was run that was identical to the 90-dB acoustic receptivity simulation except that the receptivity sight (the bump) on the plate was removed. As expected, this simulation did not produce any measurable T–S waves. Also, the boundary condition treatment proved to be robust in that this nonreceptive case yielded a temporal periodic state throughout several periods of the acoustic waves passing through the computational boundaries.

## IV. Concluding Remarks

The receptivity simulations were chosen as challenging problems to test the CFA methodology described. The code, as the embodiment of the finite compressibility solution using the boundary condition formulations outlined, performed well in both the induced and acoustic receptivity simulations. This is one of the first numerical simulations of receptivity at a localized surface inhomogeneity, which includes a realistic simulation of the acoustic wavelength. The computational expense of the acoustic receptivity simulation highlights the need for computational efficiency. An explicit time advancement scheme, which was required for these transitional instability simulations, can be optimized for vector or parallel machines. Whereas higher-order spatial discretizations may appear desirable to reduce the number of cells needed for a given level of accuracy, the minimum spatial resolution required for these viscous near-field simulations may limit the potential increase in cell size. Using an implicit method prevented convergence to an acceptable steady state. The approximately factored algorithm in conjunction with relatively high values of $\beta$ no doubt exacerbated this problem, but the potential for numerical feedback, which could transform a convective instability to a global instability, exists in any implicit (global) solution scheme. More research on applying implicit methods to convection/propagation problems is needed.

## Acknowledgments

The authors gratefully acknowledge the support of C. S. Draper Laboratories under their independent research and development and University Research support programs. Some of the computations were performed on the National Science Foundation/ Pittsburgh Supercomputing Center's Cray C90 computer under Grant CBT910018P. The authors would like to thank H. M. Atassi of the University of Notre Dame for the helpful discussions.

## References

[1]Farabee, T. M., and Geib, F. E., Jr., "Measurement of Boundary Layer Pressure Fluctuations at Low Wavenumbers on Smooth and Rough Walls," *Flow Noise Modeling, Measurement and Control* (Atlanta, GA), edited by T. M. Farabee, W. L. Keith, and R. M. Lueptow, ASME NCA-Vol. 11/FED-Vol. 130, American Society of Mechanical Engineers, New York, 1991, pp. 55–68.

[2]Morris, M. J., and McLaughlin, D. K., "Turbulent Sound Generation," *Unanswered Questions in Fluid Mechanics—1993* (New Orleans, LA), edited by L. M. Trefethen, J. A., Humphreys, and R. L. Panton, American Society of Mechanical Engineers, New York, 1993 (ASME Paper 93-WA-FE-1).

[3]Lighthill, M. J., "On Sound Generated Aerodynamically. I. General Theory," *Proceedings of the Royal Society of London, Series A: Mathematical and Physical Sciences*, Vol. 211, 1952, pp. 564–587.

[4]Mankbadi, R. R., Lyrintzis, A. S., Baysal, O., Povinelli, L. A., and Hussaini, M. Y. (eds.), *Computational Aero- and Hydro-Acoustics—1993*, ASME FED-Vol. 147, American Society of Mechanical Engineers, New York, 1993.

[5]Hardin, J. C., and Hussaini, M. Y. (eds.), *Computational Aeroacoustics*, Springer–Verlag, Berlin, 1993.

[6]Bodonyi, R. J., "Nonlinear Triple-Deck Studies in Boundary Layer Receptivity," *Applied Mechanics Reviews*, Vol. 43, No. 5 (Pt. 2), 1990, pp. S158–S165.

[7]Goldstein, M. E., "Scattering of Acoustic Waves into Tollmien–Schlichting Waves by Small Streamwise Variations in Surface Geometries," *Journal of Fluid Mechanics*, Vol. 154, 1985, pp. 509–529.

[8]Goldstein, M. E., and Hultgren, L. S., "Boundary-Layer Receptivity to Long-Wave Free-Stream Disturbances," *Annual Review of Fluid Mechanics*, Vol. 21, 1989, pp. 137–166.

[9]Kerschen, E. J., Choudhari, M., and Heinrich, R. A., "Generation of Boundary Layer Instability Waves by Acoustic and Vortical Free Disturbances," *IUTAM Laminar-Turbulent Transition Symposium Proceedings*, edited by D. Anal and R. Michel, Springer–Verlag, Berlin, 1990, pp. 478–488.

[10]Nishioka, M., and Morkovin, M. V., "Boundary-Layer Receptivity to Unsteady Pressure Gradients: Experiments and Overview," *Journal of Fluid Mechanics*, Vol. 171, 1986, pp. 219–261.

[11]Fasel, H., "Investigation of the Stability of Boundary Layers by a Finite Difference Model of the Navier–Stokes Equations," *Journal of Fluid Mechanics*, Vol. 78, Pt. 2, 1976, pp. 355–383.

[12]Fasel, H., "Numerical Simulation of Instability and Transition in Boundary Layer Flows," *IUTAM Laminar-Turbulent Transition Symposium Proceedings*, edited by D. Anal and R. Michel, Springer–Verlag, Berlin, 1990, pp. 587–598.

[13]Saric, W. S., Hoos, J. A., and Radeztsky, R. H., "Boundary-Layer Receptivity of Sound with Roughness," *Boundary Layer Stability and Transition to Turbulence* (Washington, DC), ASME FED-Vol. 114, American Society of Mechanical Engineers, New York, 1991, pp. 17–22.

[14]Chorin, A. J., "A Numerical Method for Solving Incompressible Viscous Flow Problems," *Journal of Computational Physics*, Vol. 2, No. 1, 1967, pp. 12–26.

[15]Manno, V. P., Reitsma, S. H., and Tureaud, T. F., "Developing Numerical Techniques for Solving Low Mach Number Fluid-Acoustic Problems," *AIAA Journal*, Vol. 31, No. 11, 1993, pp. 1984–1991.

[16]Reitsma, S. H., "Numerical Simulation of Low Mach Number Fluid–Acoustic Phenomena," Ph.D. Dissertation, Dept. of Mechanical Engineering, Tufts Univ., Medford, MA, Nov. 1994.

[17]Gorski, J. J., "TVD Solutions of the Incompressible Navier–Stokes Equations with an Implicit, Multigrid Technique," *Proceedings of the First National AIAA/ASME/SIAM/APS Fluid Dynamics Congress*, Vol. 1, American Physical Society, Cincinnati, OH, 1988.

[18]Roe, P. L., "Approximate Riemann Solvers, Parameter Vectors and Difference Schemes," *Journal of Computational Physics*, Vol. 43, 1981, pp. 357–372.

[19]Hedstrom, G. W., "Nonreflecting Boundary Conditions for Nonlinear Hyperbolic Systems," *Journal of Computational Physics*, Vol. 30, 1979, pp. 222–237.

[20]Thompson, K. W., "Time-Dependent Boundary Conditions for Hyperbolic Systems," *Journal of Computational Physics*, Vol. 68, 1987, pp. 1–24.

[21]Giles, M. B., "Nonreflecting Boundary Conditions for the Euler Equations," *AIAA Journal*, Vol. 28, No. 12, 1990, pp. 2050–2058.

[22]Reitsma, S. H., Manno, V. P., and Tureaud, T. F., "Non-Reflective Boundary Conditions for Fluid-Acoustic Simulations Using a Finite Volume Formulation," *Computational Aero- and Hydro-Acostics—1993* (Washington, DC), edited by R. R. Mankbadi, A. S. Lyrintzis, O. Baysal, L. A. Povinelli, and M. Y. Hussaini, ASME FED-Vol. 147, American Society of Mechanical Engineers, New York, 1993, pp. 71–82.

[23]Thompson, K. W., "Time-Dependent Boundary Conditions for Hyperbolic Systems II," *Journal of Computational Physics*, Vol. 89, 1990, pp. 439–461.

[24]Colonius, T., Lele, S. K., and Moin, P., "Boundary Conditions for Direct Computation of Aerodynamic Sound Generation," *AIAA Journal*, Vol. 31, No. 9, 1993, pp. 1574–1582.

[25]Reitsma, S. H., Manno, V. P., and Tureaud, T. F., "Simulating Receptivity Phenomena in Transitional Boundary Layer Flows," *Unsteady Flows—1994* (Lake Tahoe, NV), edited by T. Wei, W. L. Keith, and T. O. Baysal, ASME FED-Vol. 192, American Society of Mechanical Engineers, New York, 1994, pp. 1–11.

[26]Asai, M., Nishioka, M., and Suganuma, Y., "A Numerical Method for Generating Tollmien-Schlichting Waves," AIAA Paper 88-42324, 1988.

[27]Obremski, H. J., Morkovin, M. V., and Landahl, M., "A Portfolio of Stability Characteristics of Incompressible Boundary Layers," AGARD Monograph, Vol. 134, 1969.

[28]Wlezien, R. W., Parekh, D. E., and Island, T. C., "Measurement of Acoustic Receptivity at Leading Edges and Porous Strips," *Applied Mechanics Reviews*, Vol. 43, No. 5 (Pt. 2), 1990, pp. S167–S175.

[29]Choudhari, M., "Boundary Layer Receptivity in Laminar Flow Control Applications," Ph.D. Dissertation, Dept. of Aerospace and Mechanical Engineering, Univ. of Arizona, Tucson, AZ, May 1990.

S. Glegg
*Associate Editor*